Influence of doping (Ti, V, Zr, W) and annealing on the sp^2 carbon structure of amorphous carbon films

C. Adelhelm[1*], M. Balden[1], M. Rinke[2], M. Stueber[2]

[1]Max-Planck-Institut für Plasmaphysik, Materials Research, EURATOM Association, Boltzmannstraße 2, D-85748 Garching, Germany

[2]Forschungszentrum Karlsruhe, Institute of Materials Research I, Hermann-von-Helmholtz-Platz 1, D-76344 Eggenstein-Leopoldshafen, Germany

Abstract

The influence of the transition metal (Ti, V, Zr, W) doping on the carbon matrix nanostructuring during the thin film growth and subsequent annealing is investigated. Pure and metal-doped amorphous carbon films (a-C, a-C:Me) were deposited at room temperature by non-reactive magnetron sputtering. The carbon structure of as-deposited and post-annealed (up to 1300 K) samples was analyzed by X-ray diffraction (XRD) and Raman spectroscopy. The existence of graphene-like regions in a-C is concluded from a (10) diffraction peak. A comparison of the XRD and Raman results suggests that XRD probes only the small amount of 2-3 nm large graphene-like regions, whereas the majority of the sp^2 phase is present in smaller distorted aromatic clusters which are probed only by Raman spectroscopy. Annealing leads to an increase of the graphene size and the aromatic cluster size. During the carbon film growth the addition of metals enhances ordering of sp^2 carbon in sixfold aromatic clusters compared to a-C, Ti and Zr showing the strongest effect, W the lowest. This order qualitatively corresponds with the catalytic activity of the respective carbides found during graphitization of carbide-doped graphites published in the literature. With annealing, carbide

*) Corresponding author: christoph.adelhelm@ipp.mpg.de (C. Adelhelm)

crystallite formation and growth occurs in a-C:Me films, which destroys the initial carbon structure, reduces the size of the initially formed aromatic clusters and the differences in carbon structure introduced by different dopants. For high annealing temperatures the carbon structure of a-C:Me films is similar to that of a-C, and is determined only by the annealing temperature.

1. Introduction

Doping of (hydrogenated) amorphous carbon films with transition metals (a-C:Me, a-C:H:Me) is a way to improve their properties in respect to hardness, wear resistance, stress and electrical conductivity [1-6]. In nuclear fusion research, a-C:Me films are used as a model material to study the influence of metal-doping on the reactivity of carbon against hydrogen species (chemical sputtering) [7-9]. The formation of metal-containing hydrocarbon layers in fusion devices is a result of simultaneous erosion and redeposition of metallic and carbon-based plasma-facing materials (PFM) [10]. This has great importance for the next-step fusion device ITER [11], where carbon fibre reinforced carbon, tungsten and beryllium are envisaged as PFM.

In recent years several groups studied the structure of metal-containing carbon layers – mainly using Ti or W as dopant – with a focus on the bonding environment of the metal [3,12-16]. Due to the deposition conditions (high particle energy, bias voltage, elevated temperature) or high metal content (>25 %) the formation of a nanocomposite is observed with nm-sized carbide crystals embedded in a matrix of (hydrogenated) amorphous carbon. Nevertheless, for low metal contents and soft deposition conditions, the metal does not form carbide crystals detectable by X-ray diffraction (XRD) or transmission electron microscopy (TEM), and it is distributed in a mainly amorphous carbidic state in the carbon matrix [17]. Annealing can then induce the formation of carbide crystals.

For analysis of the carbon matrix in a-C:Me films, Raman spectroscopy is a common and versatile technique. Using visible laser light, a Raman spectrum is dominated by sp^2-bonded carbon due to the preferred excitation of π states. However, the spectrum depends strongly on the ordering of the sp^2 sites. Ferrari and Robertson [18] introduced a model (FR-model) to correlate the spectral features, i.e. D and G peak, to the carbon nanostructure. The G peak

around 1550 cm^{-1} is due to the in-plane bond-stretching motion of sp^2-bonded carbon atoms. This relative motion can occur for all sp^2-bonded carbon atoms in rings and chains. The D peak at ≈1360 cm^{-1} is forbidden for perfect graphite and occurs in the presence of disorder. It is only active in sixfold aromatic rings. For amorphous carbon both peaks are very broad and overlap each other, so peak fitting is essential to determine their position, width and intensity.

Assuming an amorphous carbon structure between amorphous carbon (a-C) and nanocrystalline graphite (stage 2 of the FR-model), an increase of order (e.g. by annealing) is evident by an increase of the relative D peak intensity, thus a higher I(D)/I(G) ratio. This is due to an increase in the number of 6-fold aromatic rings which cluster in small regions with size L_a. For a-C, these regions are nevertheless distorted with weak long-range order.

Ferrari and Robertson proposed the following relation between I(D)/I(G) and L_a for cluster sizes smaller than 2 nm (for an excitation laser wavelength of 514.5 nm):

$$L_a = \left[\left(I_D / I_G\right) / 0.0055\right]^{0.5} \text{Å}. \qquad (1)$$

Together with an increase of I(D)/I(G) also the G peak position is shifting towards higher wave numbers with increasing order – a result of a shortening in the average C=C double bond with higher vibration frequency. Generally, the full width at half maximum (FWHM) of D and G peak decrease with increasing order, according to the lower bonding-angle distortion.

Although Raman spectroscopy is routinely used in most investigations dealing with the structure of metal-doped amorphous carbon, only few systematic studies with different transition metals and varying metal concentrations have been performed [19]. An increase in I(D)/I(G) ratio and G peak position concomitantly with W or Ti concentration has been observed [15,20]. Abrasonis et al. [21] reported detailed about the effect of Ni-doping and substrate temperature during growth of a-C:Ni films, but the Ni concentration was fixed to 30 %.

In a-C:Me film growth, the deposition process (physical or chemical vapor deposition), kinetics and process parameters (particle energy and flux, ionization, bias voltage, temperature, pressure, sample rotation) have strong influence on the film composition and structure (metal and hydrogen content, sp^2/sp^3, sp^2 clustering, carbide formation) and therefore on the Raman spectrum. Furthermore, various methods are used to fit the Raman spectra and to derive I(D)/I(G) ratio and G peak position. This makes it difficult to compare the published data and in particular to clarify the influence of the metal type.

For this study we prepared various a-C:Me films (Me = Ti, V, Zr, W) with metal concentrations ≤19 at.%. Results from a thorough determination of the metal distribution and carbide crystallite formation (applying XRD, TEM and X-ray absorption spectroscopy,) will be published in a separate paper [22]. In the case of Ti, V and Zr doping the metal is finely dispersed in the carbon matrix in amorphous environment after deposition and exhibits a carbidic bonding state. Carbide crystallites are formed only after annealing. Indication exists for the occurrence of very small, strongly distorted tungsten carbide clusters in the as-deposited a-C:W films.

In the present paper, we report on the influence of metal type, metal concentration and annealing after deposition on the carbon phase, applying XRD and Raman spectroscopy. Based on the FR-model we show that the four metals influence the clustering of the amorphous carbon matrix to different extents during deposition. Analogous behavior of the four metals was recently observed in the catalytic graphitization strength of the corresponding carbides [23].

2. Experimental

2.1 a-C:Me film deposition and characterization

The a-C:Me films (Me = Ti, V, W, Zr) were produced by magnetron sputter deposition (Discovery 18, Denton Vacuum) using a graphite and a metal cathode [24]. No bias voltage was applied, and the sample temperature did not exceed 340 K during deposition. Ar was used as the sputtering gas, and the films (thickness varied between 0.7 and 1.5 μm) were deposited on silicon (100) wafers. Before deposition, etching of the substrate by means of a rf plasma was performed to remove the native oxide layer. The samples were annealed after deposition at 700, 900, 1100 and 1300 K in high vacuum (base pressure $\leq 5 \cdot 10^{-4}$ Pa, during heating $\leq 2 \cdot 10^{-3}$ Pa) for 15 minutes.

Rutherford backscattering spectroscopy (RBS) with 4 MeV $^4He^+$ was used to determine the depth-resolved elemental composition of the films. All concentration values are given in at.% and rounded to 0.5 %. The oxygen content was determined using films deposited on graphite substrates. An energy of 500 keV was used for surface sensitive measurements. The scattering angle was 165°, and the spectra were fitted using the program SIMNRA 6.02 [25].

Surface topography was studied by AFM in contact mode (Rasterscope 4000, AFM 2194, DME). R_q values [26] were determined on 1x1 μm^2 images at 3 different sample positions, the software Gwyddion [27] was used for image processing.

Optical reflectometry measurements were performed with a Jobin Yvon PZ 2000 ellipsometer, choosing a wavelength of 515 nm, similar to the Raman laser wavelength.

2.2 XRD

Diffractograms were measured by a Seifert XRD 3003 PTS diffractometer operating with Cu Kα radiation. The experimental setup was optimized to measure thin films in grazing incidence configuration [28]: a parabolic multilayer mirror (W/Si) was used on the primary side to achieve a parallel beam and almost complete Kβ suppression before diffraction. On the secondary side, a parallel plate collimator – oriented perpendicular to the scattering plane – was installed to prevent detection of non-parallel beam intensity. Spectra were acquired in θ-scan mode at an fixed incidence angle 1° (grazing incidence). Samples were fixed on Si wafers to exclude contributions from the sample holder during measurement. The measurement geometry results in an experimental line width of about 0.3°, determined for the Si (111) peak at 2θ = 28.4° on a powder specimen. Estimation of the (10) peak width was performed by peak fitting using PearsonVII profiles for the graphene (10) and the substrate peak at ≈53°. In the fitted range a linear background was assumed.

2.3 Raman spectroscopy

2.3.1 Measurement

Raman spectra were measured between 900 and 1900 cm^{-1} with a Renishaw 1000 microscope using an argon ion laser at 514.5 nm. The software Wire (V.1.3.18) was used to acquire the spectra, applying continuous mode and 120 s detector time. The spot size was ≈1 μm^2 and the laser power was set to 10 % giving ≈0.4 $mW/\mu m^2$, which induced no damage or structural changes in the films. This was checked visually and by applying a lower laser power which resulted in comparable spectra. For each sample, 2 or 3 spectra were recorded at different positions, which were averaged to achieve better statistics. No significant differences among the single spectra of the same sample were observed. For the given excitation energy only sp^2-bonded carbon contributes to the signal intensity. Vibrational modes of the respective metal

carbides (i.e. TiC [29] (isostructural to VC, ZrC) and tungsten carbides [30]) occur at lower wave numbers around 200 - 800 cm^{-1}.

2.3.2 Peak fitting

Different approaches using various line shapes exist for fitting Raman spectra of amorphous carbon, which can have strong influence on the derived quantitative parameters [31]. It is important to note that there is no a priori reason to favor a particular fitting function. In literature, Gaussians are common [32,33], but also asymmetrical line shapes as the Breit-Wigner-Fano (BWF) are used [18,34]. The use of an asymmetric line shape is justified by the asymmetry of the vibrational density of states (DOS) towards lower wave numbers for graphite and amorphous carbon in the region of the D and G lines [35]. Asymmetrical line shapes allow fitting the whole spectrum with only two peaks, e.g. a linear background combined with a BWF for the G peak and a Lorentzian for the D peak [18,36-38]. The strength of this combination – which was used in this work – is the increased fit quality, and one is able to fit spectra of different shapes with the same set of functions. The program fityk [39] was applied for peak fitting using the Levenberg-Marquard algorithm for non-linear least-square optimization. It provides also standard deviations for the fitted parameters.

The following expression describes the BWF line shape [18]:

$$I(\omega) = \frac{I_0\left[1+\frac{2(\omega-\omega_0)}{Q\Gamma}\right]^2}{1+\left[\frac{2(\omega-\omega_0)}{\Gamma}\right]^2} \qquad (2)$$

with $I(\omega)$ the intensity of the Raman signal at wave number ω, ω_0 as the peak position, I_0 as the peak intensity at ω_0, Γ as the full width at half maximum (FWHM) and $\frac{1}{Q}$ as the BWF

coupling coefficient. For $\frac{1}{Q} \rightarrow 0$ the line shape converge to a Lorentzian. Due to the asymmetry, the maximum of the G peak (denoted as G_{max}) is located at

$$\omega_{max} = \omega_0 + \frac{\Gamma}{2Q}. \quad (3)$$

During fitting, no constraints were used and all parameters describing the three functions were free fit variables (i.e. 2 for the linear function, 3 for the Lorentzian and 4 for the BWF). Special care was taken that the exact initial values did not affect the fit result and the global minimum during the least-square optimization was found. The I(D)/I(G) ratio was calculated using the fitted D (Lorentzian) and G (BWF) peak intensities, i.e. I_0 in Eq. (2) for the G peak.

In this paper we only discuss the development of I(D)/I(G) and G_{max}. For the sake of completeness, all parameters received from the fitting procedure are supplied as supplementary data. The error bars for all I(D)/I(G) and G_{max} values account for the uncertainty introduced by the fitting procedure. They have been derived from the standard deviations of the fitted parameters and by applying Gaussian error propagation.

3. Results

3.1 Film preparation and annealing

All investigated films show a very low surface roughness with R_q values between 2 and 4 nm. Therefore, the possible influence of surface roughness on Raman measurements can be excluded.

RBS analysis with 4 MeV $^4He^+$ confirmed the homogeneity of the deposited layer regarding composition in lateral space and within the information depth of the Raman signal, which is ≈100 nm [40]. The films contain ≈1 % Ar and 2-3 % O. After annealing at 900 K, the Ar content is reduced, vanishing completely after 1100 K. No increased oxygen content in the bulk was observed and no diffusion of carbon or metal into the substrate occurred. RBS measurements with 500 keV $^4He^+$ showed, that annealing to 1100 and 1300 K leads to slight surface enrichment of the metal in the first 10 nm for Ti, V and Zr-doped samples; also increased oxygen concentration was found in this region. Considering the information depth of the Raman signal, this effect can be neglected.

3.2 XRD

The X-ray diffractograms presented in Fig. 1a were derived for a series of a-C films annealed up to 1300 K. Measurement of a pure Si wafer proved that the broad peaks around $2\theta = 53°$ and 82° are related to the substrate. They are probably due to the thin native SiO_2 layer on top which was not completely removed during the etching procedure. Contributions from the Si wafer on which the samples were mounted are also possible. The peak around 43° originates from a-C. It is already visible with very low intensity in the as-deposited film and develops with annealing temperature, i.e. the intensity increases and the peak width decreases. This

peak should be related to two-dimensional order in graphene-like regions and therefore can be most likely assigned to the (10) reflection of a graphene plane. Annealing increases order and size of the planes as can be concluded from the increasing intensity and decreasing peak width.

A rough estimation of the graphene size was done by applying the Scherrer formula. Using a pre-factor of 1.84 (instead of 0.92, to account for scattering from 2-dimensional objects [41]) L_a values of about 2 to 3 nm were derived (see inset of Fig. 1a). The large value for as-deposited a-C is probably related to the low peak intensity which leads to high uncertainty in the determination of L_a. For the diffractograms of the 1100 and 1300 K annealed samples, also the (11) peak is visible around 80°. No reflection resulting from stacking of graphene planes (the c direction of graphite, (002)) is observed, indicating only two-dimensional order. The low intensity of the (10) peak compared to the background suggests, that only a small amount of carbon is located in graphene-like clusters that have sufficient high order for contributing to a diffraction peak.

The strong increase of the signal intensity towards lower 2θ was observed for all samples, also for the pure Si substrate and is a result of the measurement geometry. In order to determine whether intensity in the low 2θ range is also related to carbon, the diffractogram of the Si wafer was subtracted from the a-C spectra as a rough approximation. Before subtraction, the spectra were smoothed and normalized to intensity at 70°, a region appearing undisturbed from intensity related to the substrate or carbon. The resulting differences are shown in Fig. 1b. In this graph the development of the (10) peak is clearly visible, for the 1300 K diffractogram also the (11) peak is present. Negative values result from the higher intensity of the substrate-related peaks when measuring the uncoated Si wafer. In the low 2θ range around 23-25°, a broad bump can be observed which decreases in intensity with annealing (except the 900 K spectrum, see below); therefore its occurrence from a stacking of

graphene clusters is unlikely (the (002) reflection of graphite is around 2θ=26.4°). An increase in signal intensity would be expected with annealing, and therefore the feature should be related to disorder. The peak position could be an indication for scattering between 2-3 atomic distances. It is important to note that the slope around 2θ ≤ 30° in the diffractograms of Fig. 1a appeared to be very sensitive to the experimental conditions. Small deviations from a perfect planar sample alignment, different sample sizes or mounting influences the observed intensity in the low 2θ range and can therefore – after subtraction of the Si spectrum – alter the intensity and position of this broad peak in the difference plot. Therefore, a better measure for the broad feature in Fig. 1b should be the intensity at the right shoulder, e.g. around 2θ ≈ 30-35°.

The described (10) peak could only be observed for a-C, as-deposited a-C:Ti and a-C:V films with low metal content. All other a-C:Me samples (especially after annealing) showed higher background and a development of carbide peaks which overlaid the weak intensity resulting from scattering of the carbon phase. In Fig. 1b also the difference spectrum of an as-deposited 7.5 % a-C:Ti sample is included. The (10) peak appears with similar intensity as for pure a-C. This indicates that Ti-doping does not influence formation of the graphene-like regions giving rise to the observed diffraction peak.

Probably only a small fraction of carbon is located in graphene-like clusters having sufficient high order to contribute to the (10) diffraction peak. The majority of carbon atoms are assumed in a more disordered, amorphous environment and in small, distorted aromatic clusters. Raman spectroscopy is a convenient tool to study the structure of carbon materials with low long-range order. In the following section the influence of doping and annealing on the Raman spectra will be described.

3.3 Raman spectroscopy

3.3.1 Qualitative observations

As expected for amorphous carbon films, the Raman spectra of all investigated films exhibit two broad overlapping features, namely the D peak around 1360 cm^{-1} and the G peak at ≈1550 cm^{-1}. Fig. 2 shows the Raman spectra of the annealing series of pure a-C. Annealing leads to an increase of the D peak intensity and a shift of the G peak position to higher wave numbers. This is in accordance with increasing order of the carbon phase in stage 2 of the FR-model and is a result of stronger clustering of sp^2 carbon in aromatic rings (I(D)/I(G)) and a shortening of the average C=C distance (G_{max}) [18].

Fig. 3 presents Raman spectra of as-deposited a-C and a-C:Ti films doped with 1, 3.5 and 7.5 % Ti. At a first glance the most obvious difference is the significant decrease in intensity when introducing even low amounts of Ti in a-C. This is also observed for doping with V, Zr and W. Besides the possible increased light absorption in the layer due to metal incorporation and the fraction of carbon bonded to the metal, we mainly attribute this effect to increased surface reflectivity of the films due to the introduced metals. Therefore, a higher proportion of the laser beam is reflected at the surface and cannot generate a Raman signal reaching the detector. This was confirmed by measurements using optical reflectometry at 515 nm: the 7.5 % Ti-doped sample showed a 50 % higher reflectivity compared to a-C at 1900 cm^{-1}.

Another observation from Fig. 3 is, that with increasing metal concentration the relative D peak intensity (i.e. I(D)/I(G)) increases. It is obvious that due to the strongly varying signal intensities analysis of the spectra by peak fitting – as described in 2.3.2 – is essential to investigate the influence of both metal-doping and annealing on relative peak intensity, peak position and width.

3.3.2 Results of peak fitting

Before presenting the results from peak fitting of a-C and a-C:Me it should be stated that different fitting approaches have a very strong influence on the resulting I(D)/I(G). This is demonstrated by fitting the Raman spectra of a-C with two additional set of functions, which are also commonly used: 2 and 4 Gaussians (see Supplementary material).

The fits with two Gaussians show poor fit quality, especially in the range of the maxima, leading to an unsatisfactory description of the intensity of D and G peak. The relative increase of the D peak with increasing annealing temperature (which is obvious from Fig. 2) is not reflected in the calculated I(D)/I(G) values. I(D)/I(G) stays almost constant for the samples annealed from 700 to 1100 K and decreases for the 1300 K annealed specimen.

Two additional Gauss peaks around 1080-1100 cm^{-1} and 1470-1500 cm^{-1} were introduced for the fit with 4 Gaussians. The description of the spectral shape is sound, but the relative D peak increase is not reflected in the I(D)/I(G) ratio: decreasing I(D)/I(G) values are obtained with increasing temperature. Nevertheless, the basic requirement of stage 2 of the FR-model is a continuously increasing I(D)/I(G) with ordering. Decreasing I(D)/I(G) values with ordering should be observed in stage 1, i.e. the transition of nc-graphite to graphite [18]. Since our XRD measurements gave no indication of the formation of nanocrystalline graphite during annealing we assume that our films are described by stage 2 for all annealing temperatures. Therefore, it is reasonable to use the fitting procedure including BWF and Lorentz functions.

In the following we present the development of I(D)/I(G) and G_{max} dependent on metal-doping and annealing. Equation (1) relates I(D)/I(G) to a certain aromatic cluster size L_a for L_a <2 nm. Nevertheless, we will not discuss the absolute numbers, but concentrate on the qualitative trends. Zickler et al. [31] performed a thorough comparison of L_a determined by Raman spectroscopy and XRD, evaluated by the Scherrer equation and an analytical model.

They confirm the qualitative validity of equation (1), but argue that it is an oversimplification for the determination of exact values. For example, it does not take into account deviations from planar cluster surfaces, which is most likely the case for very small cluster sizes in a-C.

We first exemplarily present the influence of annealing and doping on I(D)/I(G) and G_{max} for a-C and a-C:V in detail. Then we describe the differences observed among the metals.

Fig. 4a summarizes I(D)/I(G) data obtained by the peak fitting for the a-C and V-doped samples. An estimation of the aromatic cluster size according to equation (1) is given on the right x-axis.

For a-C, annealing leads to a continuous increase of I(D)/I(G) (and therefore L_a) from 0.64 (as-deposited) to 0.98 (1300 K), which is expected for sputter-deposited a-C [18]. Considering the samples after deposition, V-doping also leads to a significant increase of I(D)/I(G) up to 1.09 for 8.5 % V. The lower value for the highest V concentration (19 %) indicates a maximum concentration between 9 and 19 % V, beyond which further doping decreases I(D)/I(G).

Annealing of a-C:V alters I(D)/I(G) in a different way as for a-C. For the 1.5 % V-doped layer annealing increases I(D)/I(G) only up to 900 K while higher temperatures do not result in a further increase. For the films containing 8.5 % V and higher, annealing has the opposite effect compared to a-C: it decreases I(D)/I(G) and therefore the aromatic cluster size.

The evolution of G_{max} is shown in Fig. 4b. For pure a-C, annealing leads to an increase in G_{max} from about 1554 cm^{-1} (after deposition) to 1587 cm^{-1} (1300 K), which is expected from the FR-model. Increasing the V content leads to an increase of G_{max} for the as-deposited samples. After every annealing step of a-C:V films, higher G_{max} values are always observed, which can be explained by temperature-induced ordering resulting in a decrease of the average C=C distance.

Therefore, annealing of a-C:V has different effects on I(D)/I(G) and G_{max}: I(D)/I(G) and the aromatic cluster size can be decreased by annealing (a-C:V films with higher V concentration), while G_{max} is always shifted to higher wave numbers. This is in contrast to pure a-C (and therefore the FR-model), for which annealing always increases the aromatic cluster size.

In annealed samples the influence of V content is a lowering of G_{max} at low V concentrations. For 3.5 % V, a minimum value is reached, while higher V concentrations increase G_{max}.

Fig. 5 summarizes I(D)/I(G) values for a-C and a-C:Me for all dopants and annealing temperatures. The data for the layers after deposition show that the metal addition generally increases I(D)/(G) and an influence of the metal type can be observed. Up to ≈4 % metal, I(D)/I(G) increases from 0.6 to ≈0.9 for Ti, V and Zr. At higher metal concentrations, doping with Ti and Zr increases I(D)/I(G) stronger than the doping with V and W, up to ≈1.6 for 14.5 % Zr. For 2.5 % W, doping results in a decrease of I(D)/I(G) compared to pure a-C, higher concentrations increase I(D)/I(G) to ≈1.1 for 14.5 % W. The similar behavior of Zr and Ti and the difference of Ti and V indicate that the effect of the different dopants on I(D)/I(G) (as-deposited samples) is not related to the atomic mass but point to a chemical influence of the metals.

With increasing the annealing temperature the differences in I(D)/I(G) vanish. I(D)/I(G) of the doped layers converge gradually to the value of pure a-C. At 1300 K they all lie between 0.9 and 1.0, the values for a-C:W at the lower end.

Fig. 6 shows the corresponding G_{max} values. Considering the data after deposition, doping with low metal concentrations leads – except for V – to a decrease of G_{max} compared to pure a-C. For higher concentrations, G_{max} generally increases for Ti, V and Zr. The 700 K data shows the appearance of a minimum in G_{max} with doping even more clearly for all dopants. With one exception (19 % V), G_{max} is generally below the value for a-C up to 900 K. Similar

to the development of I(D)/I(G), also the differences in the position of G_{max} are reduced with increasing annealing temperature. For 1100 and 1300 K, all values are similar to those of a-C and higher than those for all as-deposited films.

4. Discussion

From XRD data in Fig. 1 the existence of small graphene-like regions in pure a-C can be concluded. They have sufficient high order to lead to an occurrence of the (10) diffraction peak, and gain in size with annealing. The occurrence of stacked graphenes, i.e. small graphite crystallites, is unlikely due to the decrease of intensity at $2\theta \approx 30°$ with annealing (Fig. 1b). Cho et al. [42] analyzed the surface of sputtered a-C using STM and reported about the existence of distorted graphite crystallites (L_a= 2-4 nm). Therefore, it can not be excluded that strong distortion and small size of these crystallites might be responsible for the absence of the (002) peak from interlayer scattering.

Evaluation of the (10) peak shows an increasing average graphene size L_a from 2 to 3 nm with annealing. For L_a >2 nm, the FR-model (stage 1) predicts the cluster size to be inversely proportional to I(D)/I(G), as proposed by Tuinstra and Koenig [43]. This was not found for the annealing series of a-C (under the reasonable assumption that the cluster size increases with annealing temperature): Fig. 2 shows increasing I(D)/I(G) with temperature. An explanation of this discrepancy could be the overestimation of L_a by XRD due to the fact that the (10) peak broadening is not only determined by the small graphene size – which is the basic requirement for the application of the Scherrer formula – but also by other factors, e.g. distortion, strain. Zickler et al. [31] reported about too large size values resulting from the simple application of the Scherrer formula compared to model calculations.

Also another explanation is possible if we assume a broad L_a size distribution: the diffraction patterns in Fig. 1 are then related to >2 nm large, well-ordered graphene-like regions, but with very low occurrence. Therefore, the Raman D peak is dominated by the huge amount of smaller aromatic clusters, which do not contribute to the diffractograms because of too small size and disorder. Annealing increases the average L_a, but still the main part of the sp^2 phase is in clusters <2 nm in size, which dominates the Raman signal.

The D peak is related to the occurrence of aromatic rings, whereas a minimum size and sufficient high order of the aromatic regions are required to observe a diffraction peak. Hence, the information supported by XRD is probably not representative for the overall structural situation in a-C. In the following we will distinguish the sp^2 phase in aromatic clusters (probed only by Raman) and graphene-like clusters (probed by Raman and XRD). It has to be kept in mind that even if the structure of amorphous carbon has been studied for decades, no final model has been developed and the discussion is still lively [18,38,44-47]. Most likely the majority of the sp^2 phase in sputter-deposited a-C is located in distorted aromatic ring-systems, but also chain-like structures and non-aromatic ring systems can occur. For the a-C films used in this study an sp^2 fraction of about 80 % was estimated for the as-deposited sample, it increases up to ≈95 % after annealing to 1300 K [48].

Addition of small amounts of Ti or V does not significantly affect the (10) diffraction peak of the as-deposited samples (Fig. 1b), but it strongly alters the respective Raman spectra: generally increasing I(D)/I(G) values are observed (Fig. 5), indicating increasing L_a. This discrepancy of XRD and Raman results supports the addressed interpretation that a broad size distribution of L_a exists, and both techniques probe different parts of the sp^2 phase. The small amount of metal does not influence the few well-ordered graphene-like clusters probed by XRD, but it promotes clustering of the sp^2 phase in small, distorted aromatic clusters.

This effect is dependent on the dopant metal: Ti and Zr promote clustering of sp^2 hybridized carbon in aromatic rings stronger than V, and W has the smallest effect. Low W concentrations even decrease the cluster size compared to a-C. Therefore, the following order of the metals in promoting aromatic clustering during deposition can be made: W < V < Ti ≈Zr.

A catalytic effect of transition metals was observed during annealing experiments of a-C:Me films with high metal content or carbon-metal sandwich layers which transforms amorphous

carbon into “graphite-like” carbon [49-52]. The ability of the metals to act as catalysts is often explained by the formation of a metastable carbide phase which decomposes into a stable carbide and graphite. Nevertheless, Abrasonis et al. found for a-C:Ni films an enhanced aromatic clustering independently from the Ni phase state [21]. The importance of metals acting as catalysts in the synthesis of carbon nanotubes [53-55] and other graphitic materials [56-58] is well known even if there is still discussion about the mechanism.

Garcia-Rosales et al. [23] investigated the catalytic effect of four carbides (TiC, VC, ZrC, WC) for the production of carbide-doped fine grain graphites with high thermal conductivity. In this study, µm-sized carbide particles have been mixed with the carbon raw material (a powder of meso-carbon microbeads), resulting in an overall metal concentration of 4 at%. The carbide addition improved the thermomechanical properties after graphitization (> 2900 K) in respect to the undoped graphite. XRD measurements of the graphitic crystallite height L_c was used as a measure for the catalytic graphitization strength, which gave the following order: WC < VC < TiC < ZrC. The reason for the different graphitization strength is not clear.

The qualitative correspondence in graphitization strength of the metal carbides found by Garcia-Rosales et al. [23] and the ability of the metals to promote aromatic clustering during a-C:Me film growth (Fig. 5) is obvious. We attribute this similarity to the fact that a basic requirement of this catalytic effect is a certain atom mobility during the ordering process. During graphitization of the carbide-doped graphites this mobility is enabled by the high temperature which is above the eutectic temperature and which enables the bulk diffusion. This makes it likely that a liquid phase plays a key role according to the dissolution-precipitation mechanism [58]. During sputter deposition of a-C:Me films, atom mobility is mainly due to surface diffusion.

Carbon atom surface diffusion on metal-based particles is proposed to be a key step during carbon nanotube growth for the formation of graphitic structures [55] and is believed to be also

responsible for enhanced aromatic clustering during growth of a-C:Ni films [21]. In comparison, the metal content of our films is relatively low and no metallic or carbide particles are formed during deposition [17,22]. Nevertheless, metal addition during a-C:Me film growth leads to increased aromatic clustering. Therefore, a catalytic activity during surface diffusion of the metal atoms could also be responsible for the observed effect. No correlation exists with the additional energy deposited on the growing film surface by reflected Ar ions from the metal targets which could possibly be responsible for enhanced carbon clustering. This influence would be proportional to the atomic mass of the target metal, which is not observed.

The lowest ordering effect of tungsten in a-C:W might be explained by the rapid formation of very small, strongly distorted carbide crystallites already during deposition. XRD and EXAFS measurements suggest for the as-deposited Ti, V (except 19 %), and Zr-doped films mainly an amorphous environment without formation of nm-sized carbide crystallites, whereas in a-C:W films XRD indicates strongly distorted carbide cluster formation already during deposition [22]. This crystallite formation could lead to a decreased mobility of W through the carbon matrix during film growth and to a deactivation of metal inside the carbide. Therefore, the catalytic effect is reduced. The formation of carbide crystallites already during deposition is also found for the 19 % V doped sample. This could explain the decrease of I(D)/I(G) compared to the a-C:V film with 8.5 % V (Fig. 4).

The similar ordering effect of the metals on the carbon structure during a-C:Me film growth and during the production of fine grain graphites [23] point to a basic influence of the metal type, which has to be further studied.

Annealing of a-C:Me films after deposition reduce the differences in I(D)/I(G) as shown in Fig. 5. In contrast to a-C, post-annealing of a-C:Me films decreases the average aromatic cluster size compared to the as-deposited samples. This can be explained by successive formation and growth of carbide crystallites due to annealing. Carbide crystallite growth

requires diffusion of metal atoms through the a-C phase which destroys the initial carbon structure formed. The mobility of the metal atoms during this process is much smaller than during layer formation by sputtering. Ordering of the a-C phase is therefore more and more determined by the annealing temperature. After annealing to 1300 K, the similar I(D)/I(G) values can be explained by the formation of a composite of nm-sized carbide crystallites in the a-C phase. The average aromatic cluster size in 1300 K annealed a-C and a-C:Me films is therefore only affected by the annealing temperature.

The influence of metal-doping on G_{max} for the samples after deposition and heated to 700 K (Fig. 6) is ambiguous and cannot be fully explained. For low metal contents the lowering of G_{max} compared to a-C indicate higher bond disorder [18]. A further increase of the metal content shifts G_{max} to higher wave numbers, indicating higher bond order. This is in contrast to the development of I(D)/I(G) which generally increases for higher metal concentration. It has to be noted that up to a temperature of 900 K most G_{max} values of a-C:Me films are well below the values of pure a-C (Fig. 6), which indicates that doping results in higher bond distortion even if sp^2 clustering is enhanced. It could be speculated that also another effect could play a role if we bring to mind that the relative motion of connected sp^2 carbon atoms is responsible for the G peak. Metal atoms in the neighborhood of sp^2 sites could slow down the relative sp^2 movement due to their inertia, lowering the G_{max} position. Nevertheless, this explanation and also the possible influence of heavy atoms on the vibrational modes of an adjacent C=C bond need further investigation.

Increasing the annealing temperature diminishes the differences in G_{max} position. In contrast to the development of I(D)/I(G) annealing leads generally to higher G_{max} values according to the FR-model for increasing order. This indicates that even if temperature-induced metal diffusion and growth of carbide crystallites decreases the average aromatic cluster size a higher local C=C bond order results by annealing.

5. Conclusion

In this work we investigated the influence of a) doping with transition metals (Ti, V, Zr, W) and b) annealing after deposition on the carbon structure using XRD and Raman spectroscopy. Comparison of both techniques suggests that a broad size distribution of aromatic regions exist. XRD is sensitive for only the small amount of large and well-ordered graphene-like clusters. The majority of the sp^2 phase is probably present in small, distorted aromatic clusters which are probed only by Raman spectroscopy. During sputter deposition of a-C:Me films the metal does not seem to influence the formation of the small amount of large and well-ordered graphene-like regions, as measured by XRD for a 7.5 % Ti-doped sample. But metal-doping shows a significant promoting effect on sp^2 clustering in small aromatic regions during deposition, which is dependent on the type of metal. W-doping shows the lowest influence, whereas Ti and Zr-doping has the highest effect on promoting sp^2 clustering. The different behavior of the metals qualitatively corresponds to the catalytic graphitization strength of the respective carbides in the production of carbide-doped graphites found by Garcia-Rosales et al. [23]. A decreased bond ordering compared to a-C is found for the doped films up to 900 K. With annealing, metal diffusion and successive formation of nm-sized carbide crystallites lead to a carbon structure which is determined by the annealing temperature only, independent of dopant metal and concentration.

6. Acknowledgements

C.A. would like to thank F. Koch, and U. von Toussaint for helpful discussions and T. Schwarz-Selinger for the performance of reflectometry measurements. T. Dürbeck is acknowledged for annealing samples, H. Lee for manuscript corrections.

Part of this work has been performed within the framework of the Integrated European Project "Extremat" (contract NMP-CT-2004-500253) with financial support by the European Community. It only reflects the view of the authors and the European Community is not liable for any use of the information contained therein.

References

[1] A. A. Voevodin, S. V. Prasad, and J. S. Zabinski, Journal Of Applied Physics **82,** 855 (1997).

[2] C. Corbella, G. Oncins, M. A. Gomez, M. C. Polo, E. Pascual, J. Garcia-Cespedes, J. L. Andujar, and E. Bertran, Diamond and Related Materials **14,** 1103 (2005).

[3] E. Lewin, O. Wilhelmsson, and U. Jansson, Journal of Applied Physics **100,** 054303 (2006).

[4] D. Nilsson, F. Svahn, U. Wiklund, and S. Hogmark, Wear **254,** 1084 (2003).

[5] Y. T. Pei, D. Galvan, and J. T. M. De Hosson, Journal of Vacuum Science & Technology A **24,** 1448 (2006).

[6] W. J. Meng and B. A. Gillispie, Journal of Applied Physics **84,** 4314 (1998).

[7] M. Balden, J. Roth, E. D. Pardo, and A. Wiltner, Journal Of Nuclear Materials **313,** 348 (2003).

[8] M. Balden, E. D. Pardo, I. Quintana, B. Cieciwa, and J. Roth, Journal of Nuclear Materials **337-39,** 980 (2005).

[9] M. Balden and C. Adelhelm, Physica Scripta **T128,** 121 (2007).

[10] R. P. Doerner, Journal of Nuclear Materials **363-365,** 32 (2007).

[11] Y. Shimomura, Journal of Nuclear Materials **363-365,** 467 (2007).

[12] W. J. Meng, R. C. Tittsworth, J. C. Jiang, B. Feng, D. M. Cao, K. Winkler, and V. Palshin, Journal of Applied Physics **88,** 2415 (2000).

[13] B. Feng, D. M. Cao, W. J. Meng, J. Xu, R. C. Tittsworth, L. E. Rehn, P. M. Baldo, and G. L. Doll, Surface & Coatings Technology **148,** 153 (2001).

[14] A. Y. Wang, K. R. Lee, J. P. Ahn, and J. H. Han, Carbon **44,** 1826 (2006).

[15] S. J. Park, K. R. Lee, D. H. Ko, and K. Y. Eun, Diamond and Related Materials **11,** 1747 (2002).

[16] A. A. Voevodin, J. P. O'Neill, S. V. Prasad, and J. S. Zabinski, Journal of Vacuum Science & Technology A **17,** 986 (1999).

[17] C. Adelhelm, M. Balden, and M. Sikora, Materials Science and Engineering: C **27,** 1423 (2007).

[18] A. C. Ferrari and J. Robertson, Physical Review B **61,** 14095 (2000).

[19] E. A. Smorgonskaya and V. I. Ivanov-Omskii, Semiconductors **39,** 934 (2005).

[20] S. Zhang, X. L. Bui, J. Jiang, and X. M. Li, Surface & Coatings Technology **198,** 206 (2005).

[21] G. Abrasonis, M. Krause, A. Mucklich, K. Sedlackova, G. Radnozi, U. Kreissig, A. Kolitsch, and W. Moller, Carbon **45,** 2995 (2007).

[22] C. Adelhelm, M. Balden, M. Rasinski, and M. Sikora, in preparation.

[23] C. Garcia-Rosales, N. Ordas, E. Oyarzabal, J. Echeberria, M. Balden, S. Lindig, and R. Behrisch, Journal Of Nuclear Materials **307,** 1282 (2002).

[24] M. Balden, B. T. Cieciwa, I. Quintana, E. de Juan Pardo, F. Koch, M. Sikora, and B. Dubiel, Surface and Coatings Technology **200,** 413 (2005).

[25] M. Mayer, "SIMNRA User's Guide, Tech. Rep. IPP 9/113," (1997).

[26] E. S. Gadelmawla, M. M. Koura, T. M. A. Maksoud, I. M. Elewa, and H. H. Soliman, Journal of Materials Processing Technology **123,** 133 (2002).

[27] http://gwyddion.net/.

[28] M. Birkholz, *Thin Film Analysis by X-Ray Scattering* (Wiley-VCH Weinheim, 2006).

[29] M. V. Klein, J. A. Holy, and W. S. Williams, Physical Review B **17,** 1546 (1978).

[30] B. Q. Yang, X. P. Wang, H. X. Zhang, Z. B. Wang, and P. X. Feng, Materials Letters **62,** 1547 (2008).

[31] G. A. Zickler, B. Smarsly, N. Gierlinger, H. Peterlik, and O. Paris, Carbon **44,** 3239 (2006).

[32] R. Gago, M. Vinnichenko, H. U. Jager, A. Y. Belov, I. Jimenez, N. Huang, H. Sun, and M. F. Maitz, Physical Review B **72,** 014120 (2005).

[33] H. X. Li, T. Xu, C. B. Wang, J. M. Chen, H. D. Zhou, and H. W. Liu, Thin Solid Films **515,** 2153 (2006).

[34] S. Prawer, K. W. Nugent, Y. Lifshitz, G. D. Lempert, E. Grossman, J. Kulik, I. Avigal, and R. Kalish, Diamond and Related Materials **5,** 433 (1996).

[35] R. O. Dillon, J. A. Woollam, and V. Katkanant, Physical Review B **29,** 3482 (1984).

[36] D. G. McCulloch, S. Prawer, and A. Hoffman, Physical Review B **50,** 5905 (1994).

[37] C. Lenardi, P. Piseri, V. Briois, C. E. Bottani, A. L. Bassi, and P. Milani, Journal of Applied Physics **85,** 7159 (1999).

[38] G. Abrasonis, R. Gago, M. Vinnichenko, U. Kreissig, A. Kolitsch, and W. Moller, Physical Review B **73** (2006).

[39] http://www.unipress.waw.pl/fityk/.

[40] Y. Lifshitz, Diamond and Related Materials **12,** 130 (2003).

[41] B. E. Warren, Physical Review **59,** 693 (1941).

[42] N. H. Cho, D. K. Veirs, J. W. Ager, M. D. Rubin, C. B. Hopper, and D. B. Bogy, Journal of Applied Physics **71,** 2243 (1992).

[43] F. Tuinstra and J. L. Koenig, Journal of Chemical Physics **53,** 1126 (1970).

[44] J. Diaz, S. Anders, X. Zhou, E. J. Moler, S. A. Kellar, and Z. Hussain, Physical Review B **64,** 125204 (2001).

[45] J. C. Han, W. Gao, J. Q. Zhu, S. H. Meng, and W. T. Zheng, Physical Review B **75** (2007).

[46] J. Diaz, O. R. Monteiro, and Z. Hussain, Physical Review B **76** (2007).

[47] J. Robertson and E. P. Oreilly, Physical Review B **35,** 2946 (1987).

[48] C. Adelhelm, M. Balden, F. Kost, A. Herrmann, and S. Lindig, Journal of Physics: Conference Series **100,** 062033 (2008).

[49] R. Sinclair, T. Itoh, and R. Chin, Microscopy and Microanalysis **8,** 288 (2002).

[50] A. G. Ramirez, T. Itoh, and R. Sinclair, Journal Of Applied Physics **85,** 1508 (1999).

[51] T. J. Konno and R. Sinclair, Acta Metallurgica Et Materialia **42,** 1231 (1994).

[52] T. J. Konno and R. Sinclair, Acta Metallurgica Et Materialia **43,** 471 (1995).

[53] P. J. F. Harris, Carbon **45,** 229 (2007).

[54] A. Gorbunov, O. Jost, W. Pompe, and A. Graff, Carbon **40,** 113 (2002).

[55] S. Hofmann, G. Csanyi, A. C. Ferrari, M. C. Payne, and J. Robertson, Physical Review Letters **95** (2005).

[56] M. Sevilla and A. B. Fuertes, Carbon **44,** 468 (2006).

[57] F. J. Maldonado-Hodar, C. Moreno-Castilla, J. Rivera-Utrilla, Y. Hanzawa, and Y. Yamada, Langmuir **16,** 4367 (2000).

[58] A. Oya and H. Marsh, Journal of Materials Science **17,** 309 (1982).

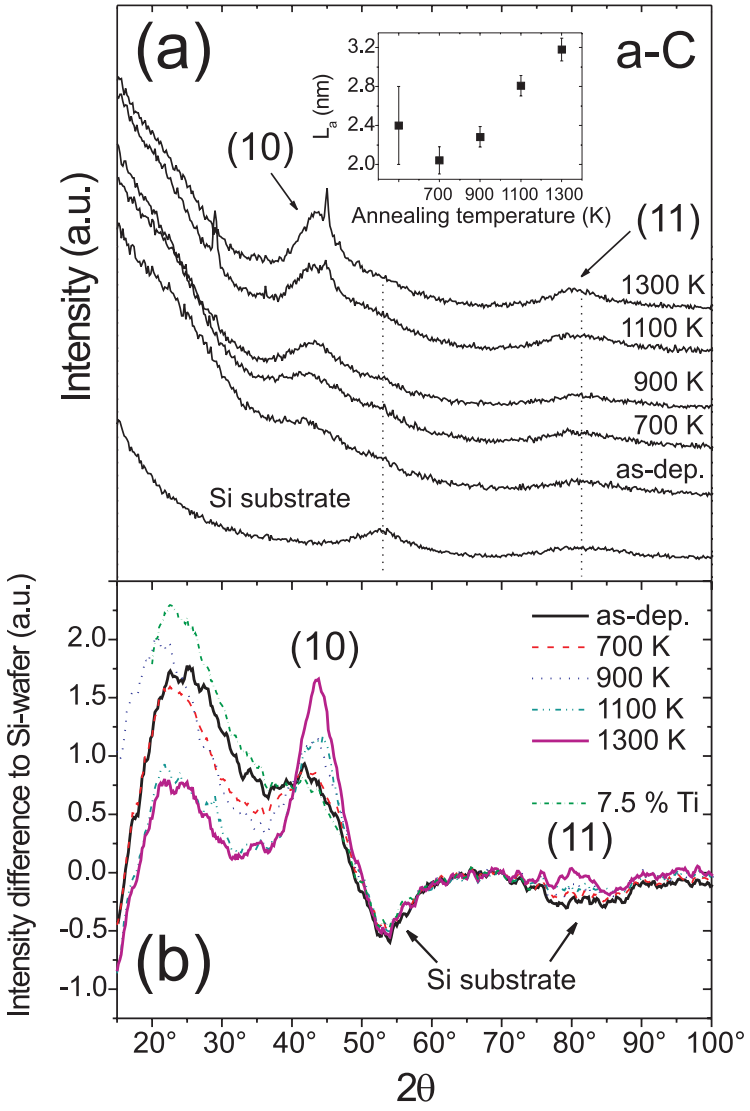

Fig. 1: a) XRD patterns of the annealing series of a-C. A diffractogram of an uncoated silicon wafer is given at the bottom. Spectra are shifted vertically for clarity purposes. The graphenic cluster size L_a calculated by applying the Scherrer formula to the (10) peak is presented in the inset. b) Remaining intensity of a-C and a-C:Ti (7.5 % Ti, as-deposited) diffractograms after subtraction of the diffractogram of the Si substrate. Before subtraction, spectra were smoothed and normalized to the intensity at 70°.

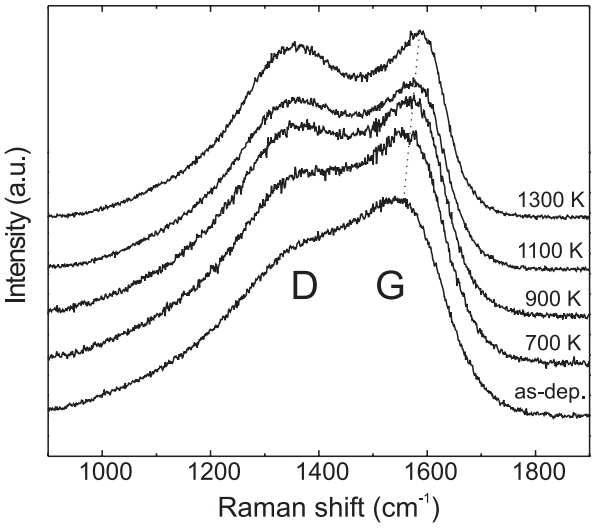

Fig. 2: Raman spectra of a-C films after deposition and post-annealing for 15 minutes at 700, 900, 1100 and 1300 K. The spectra are vertically shifted. To guide the eye, the shift in G position is emphasized by a line.

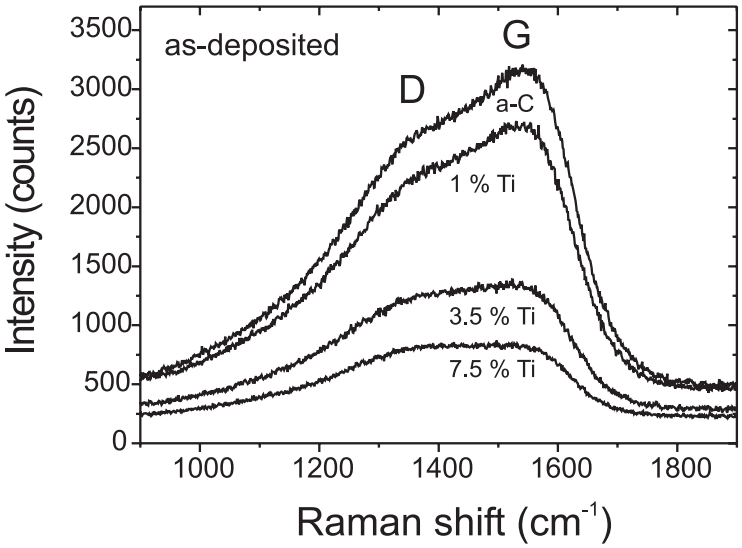

Fig. 3: Raman spectra of the as-deposited a-C and a-C:Ti films with 1, 3.5 and 7.5 % Ti.

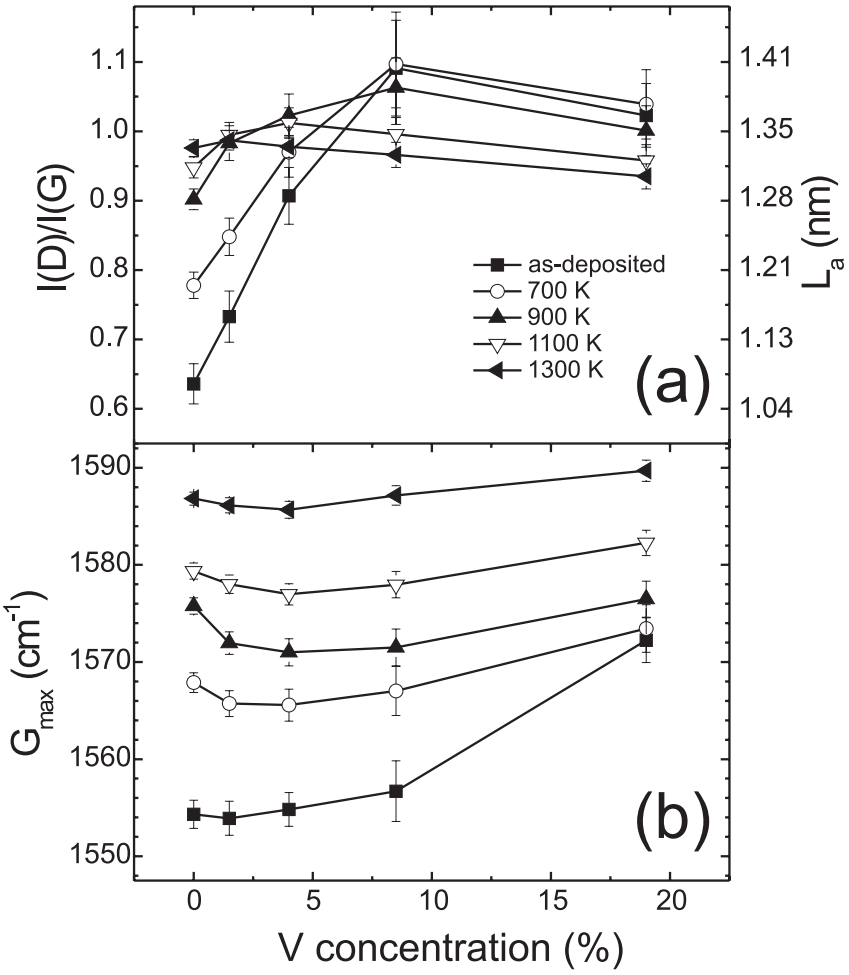

Fig. 4: a) I(D)/I(G) and b) G_{max} for a-C: and a-C:V samples after deposition and annealing at different temperatures. On the right axis of the panel (a) the estimated aromatic cluster size according to equation (1) is given.

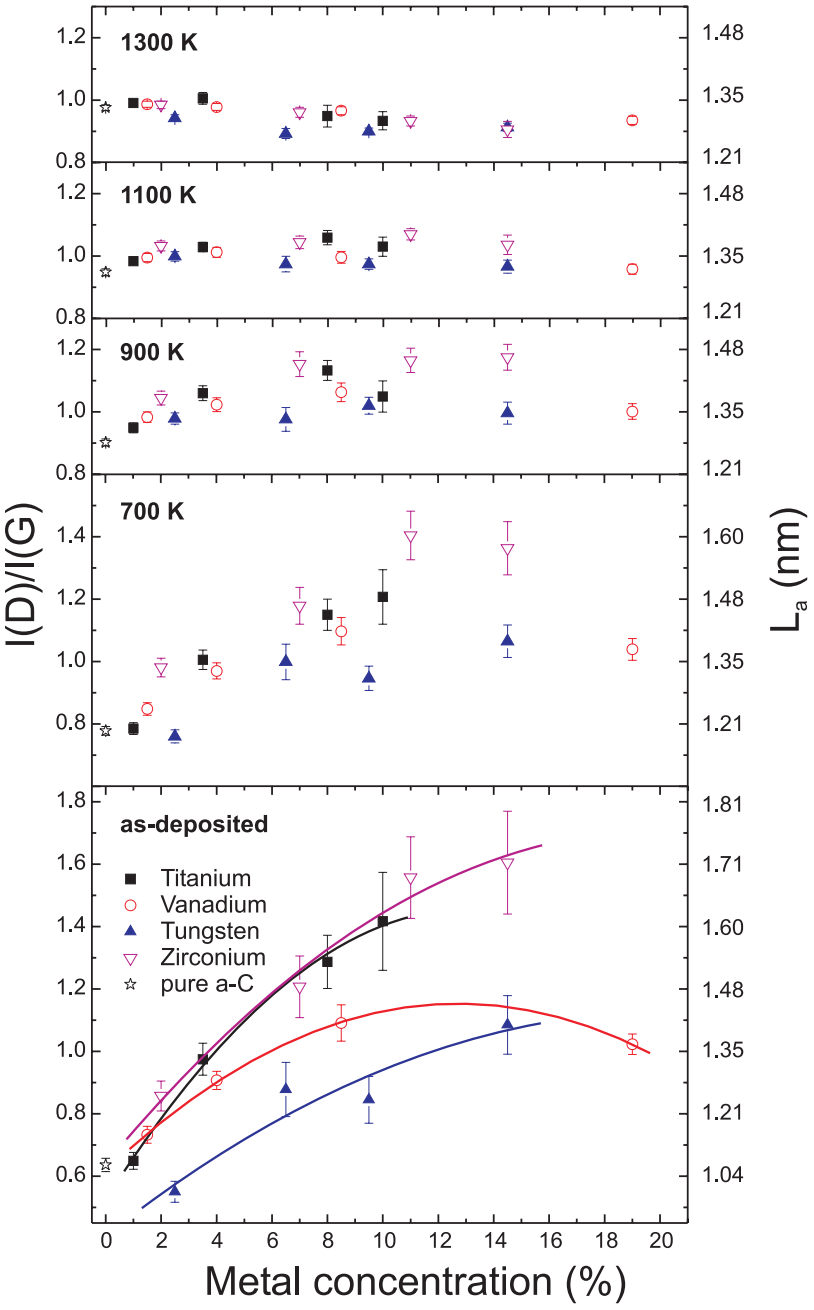

Fig. 5: I(D)/I(G) for all the investigated layers after deposition and annealing at different temperatures as indicated in the panels. On the right axis the estimated aromatic cluster size according to equation (1) is given. The curves in the bottom graph are only to guide the eye. The range of the y-scale is adjusted keeping the same stepwidth.

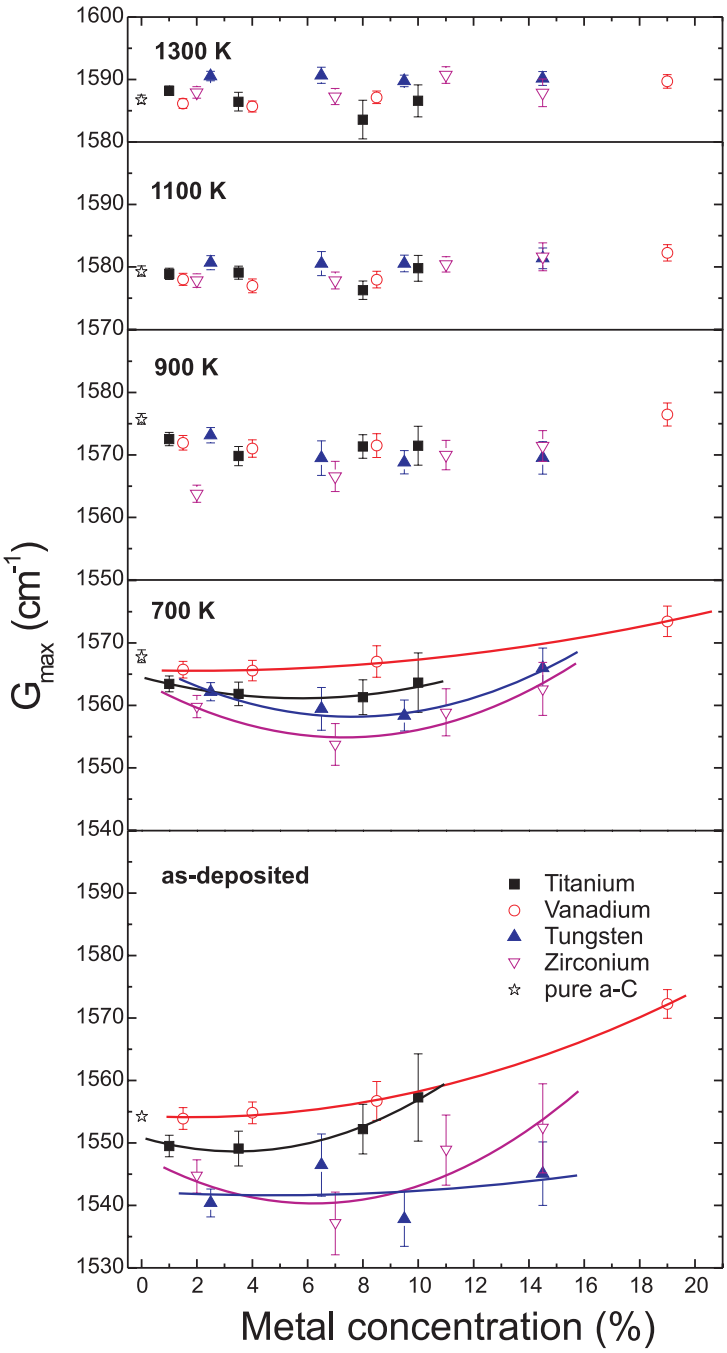

Fig. 6: G_{max} values for all investigated layers after deposition and annealing at different temperatures as indicated in the panels. The curves are only to guide the eye. The range of the y-scale is adjusted keeping the same stepwidth.